

# Role of interface shape on the laminar flow through an array of superhydrophobic pillars

Jeong-Hyun Kim<sup>1</sup> · Jonathan P. Rothstein<sup>1</sup>

Received: 22 March 2017 / Accepted: 3 April 2017 / Published online: 8 April 2017  
© Springer-Verlag Berlin Heidelberg 2017

**Abstract** In this study, measurements of the pressure drop and the velocity vector fields through a regular array of superhydrophobic pillars were systematically taken to investigate the role of air–water interface shape on laminar drag reduction. A polydimethylsiloxane microfluidic channel was created with a regular array of apple-core-shaped and circular pillars bridging across the entire channel. Due to the shape and hydrophobicity of the apple-core-shaped pillars, air was trapped on the side of the pillars after filling the microchannel with water. The measurements were taken at a capillary number of  $Ca = 6.6 \times 10^{-5}$ . The shape of the air–water interface trapped within the superhydrophobic apple-core-shaped pillars was systematically modified from concave to convex by changing the static pressure within the microchannel. The pressure drop through the microchannel containing the superhydrophobic apple-core-shaped pillars was found to be sensitive to the shape of the air–water interface. For static pressures which resulted in the apple-core-shaped superhydrophobic pillars having a circular cross section,  $D/D_0 = 1$ , a drag reduction of 7% was measured as a result of slip along the air–water interface. At large static pressures, the interface was driven into the apple-core-shaped pillars, resulting in decrease in the effective size of the pillars and an increase in the effective spacing between pillars. When combined with a slip velocity measured to be 10% of the average velocity between the pillars, the result was a pressure drop reduction of 18% compared to the circular pillars at a non-dimensional

interface diameter of  $D/D_0 = 0.8$ . At low static pressures, the pressure drop increased significantly as the expanded air–water interface constricted flow through the array of pillars even as large interfacial slip velocity was maintained. At  $D/D_0 = 1.1$ , for example, the pressure drop increased by 17% compared to the circular pillar. This drag increase was the result of an increased form drag due to a decrease in porosity and permeability of the pillar array and a decrease in the skin friction drag due to the presence of the air–water interface. For  $D/D_0 = 1.1$ , the slip velocity was measured to be 45% of the average streamwise velocity between the pillars. When compared to no-slip pillars of similar shape, the drag reduction was found to increase from 6 to 9% with increasing convex curvature of the air–water interface.

**Keywords** Superhydrophobic surface · Pressure drop · Particle image velocimetry

## 1 Introduction

As a solid object moves through a fluid, it will invariably experience a resistance force or a drag. Drag increases operational cost of ships, automobiles, and pipelines. As a result, reducing drag in fluid flow has been one topic of study in the field of fluid dynamics. In internal flows like those through pipes, for example, a number of different strategies have been utilized to reduce the shear stress along the pipe wall including the addition of high molecular weight polymers to the flow (White and Mungal 2008), the injection of air bubbles near the surface of the pipe (Elbing et al. 2008; Sanders et al. 2006), and the introduction of small-scale structures to a hydrophobic wall to trap air between surface features and make the surface superhydrophobic (Daniello et al. 2009; Ou

✉ Jonathan P. Rothstein  
rothstein@ecs.umass.edu

<sup>1</sup> Department of Mechanical and Industrial Engineering,  
University of Massachusetts Amherst, 160 Governors Drive,  
Amherst, MA 01003-2210, USA

et al. 2004; Watanabe et al. 1999). Among those methods, the use of superhydrophobic surfaces for drag reduction has been spotlighted over the last two decades (Rothstein 2010).

Superhydrophobic surfaces are hydrophobic surfaces containing micron-/nanometer-sized surface roughness. Due to the combination of chemical hydrophobicity and structural topography, an air layer is created between peaks of surface roughness. It results in the formation of an air–water interface along the superhydrophobic surfaces. The presence of the air–water interface can make the surface extremely non-wetting, can result in an increase in the advancing contact angle with water toward  $180^\circ$ , and can mobilize drops by reducing the contact angle hysteresis of the surface to  $0^\circ$  (Kim et al. 2015; Rothstein 2010). The presence of the air–water interface has also been shown to generate both laminar and turbulent drag reduction by introducing a nonzero slip velocity along the trapped and nearly shear-free air–water interface (Choi and Kim 2006; Daniello et al. 2009; McHale et al. 2009; Ou et al. 2004; Song et al. 2014; Srinivasan et al. 2013; Truesdell et al. 2006; Watanabe et al. 1999). The drag reduction produced by a superhydrophobic surface depends on the dimensions of the pipe or channel, the fraction of the superhydrophobic surface covered by an air–water interface, and the size and spacing of the surface features (Oner and McCarthy 2000; Ou et al. 2004; Rothstein 2010; Song et al. 2014). Maximum drag reduction is achieved with decreasing channel height, increasing air–water interface coverage and larger feature spacing (Ou et al. 2004). The existence of a nonzero slip velocity at the air–water interface has been demonstrated through micro-PIV ( $\mu$ PIV) measurements and numerical simulations (Ou and Rothstein 2005; Tsai et al. 2009).

There have also been a number of studies investigating how superhydrophobicity and slip can affect flow past two- and three-dimensional bodies like hydrofoils (Balasubramanian et al. 2004; Gogte et al. 2005), spheres (McHale et al. 2009), and cylinders (Daniello et al. 2013; Legendre et al. 2009; Muralidhar et al. 2011; You and Moin 2007). Here, we will present pressure drop and velocity vector field results for the flow through a periodic array of cylindrical pillars whose cross-sectional shape and surface topography were designed to trap air and thereby making them superhydrophobic. Unlike previous studies on three-dimensional bodies, in these experiments, the size of the pocket of trapped air will be comparable to the size of the cylinder making it easily observable under the microscope. Additionally, we will show that by using variations in static pressure, the shape and extent of the trapped air against the superhydrophobic pillar can be modified to control the shape of the pillars along with the permeability and porosity of the periodic array of pillars.

In most previous studies, the air–water interface trapped within the superhydrophobic surface was assumed to be flat. However, at large flow rates and pressures, the interface can be deformed and eventually driven into the surface features and lost. Thus, understanding the role of interface shape on the performance of superhydrophobic surfaces is extremely important if the performance of the surfaces is to be fully optimized. The theoretical deflection of the air–water interface can be determined by the difference in the static pressure between the water and the air phases and spacing between surface roughness,  $P_{\text{water}} - P_{\text{air}} = 2\sigma_w \cos(\pi - \theta)/l$  (Rothstein 2010). Here,  $\sigma_w$  is surface tension of the water,  $l$  is spacing between surface roughnesses,  $\theta$  is deflection angle of the interface from the flow direction, and the deflection is assumed to drive the interface into a circular hole. As the static pressure in the water phase is increased through an increase in the flow rate and/or a decrease in the channel height, the deflection angle of the interface increases but remains pinned to the top of the surface roughness until it reaches the local advancing contact angle. As a result, the air–water interface is driven further and further into the surface as pressure in the water compresses the air phase, giving the interface a concave shape. At a large enough water pressure, the advancing contact angle is reached and the air–water interface collapses, eliminating the drag reducing properties of the superhydrophobic surfaces. Conversely, a convex interface shape can also be achieved by decreasing the static pressure of the water phase or increasing the static pressure of the air phase.

In laminar flows, it has been shown that the continuity and shape of the air–water interface is an important factor in drag reduction. Steinberger et al. (2007) used a modified SFA to investigate the hydrodynamics of a water glycerol mixture confined between a sphere and a superhydrophobic surface containing a square array of  $d = 1.3 \mu\text{m}$  holes to form a “bubble mattress.” Isolated bubbles have been shown both experimentally and numerically to perform relatively poorly for drag reduction because the air–water interface that is formed is not continuous along the surface and large slip velocities cannot be obtained (Davis and Lauga 2009). The experimental measurements of Steinberger et al. (2007) actually showed that a larger slip length was achieved for the hydrophilic, fully wetted holes in the Wenzel state,  $b \approx 105 \text{ nm}$ , then the hydrophobic Cassie state,  $b \approx 20 \text{ nm}$ . To understand why, the authors performed a series of numerical simulations where they studied the effect of interface shape on the resulting slip length. They found that the maximum drag reduction was achieved when the air–water interface supported above the holes was flat and dropped off quite significantly for menisci

that protruded into the flow or into the holes. Similar unexpectedly small drag reduction results were found by Bolognesi et al. (2014) for menisci that were driven into long rectangular surface cavities. However, in their case, they speculated that the decreased drag reduction was due to surface impurities and the Marangoni flow that is induced by the resulting the surface tension gradients.

The theoretical predictions of Sbragaglia and Prosperetti (2007) found similar results for the flow past microridges supporting deformed interfaces. Steinberger et al. (2007) showed that it is the immobility of the air–water interface and the resulting blockage of the flow that combine to actually enhance drag for bubbles protruding beyond the hole at an angle greater than  $\theta > 60^\circ$ . These results are in agreement with Richardson’s early predictions (Richardson 1973) that the proper macroscopic boundary condition to use for a perfectly shear-free surface will become no-slip if the surface is sufficiently rough. To date, no experiments have been performed to confirm these results for superhydrophobic surfaces which produce significant drag reduction like arrays of microridges or microposts where the interface is mobile; however, work with bubble matrices has continued to evolve experimentally.

Tsai et al. (2009) experimentally measured the shape of the air–water interface using confocal microscopy. Through micro-PIV measurements, they found that a concave air–water interface reduces the slip length from that measured on a flat interface (Tsai et al. 2009). Their follow-up research demonstrated the role of the interface geometry on the slippage over a wide range of protrusion angle from a bubble mattress (Karatay et al. 2013). An active control of the static pressure within the air phase was used to modify the protrusion angle of the interface. A maximum drag reduction of 21% and an equivalent slip length of 5  $\mu\text{m}$  were obtained at the protrusion angle of  $10^\circ$  (Karatay et al. 2013). This slip length decayed quickly for protrusion angles beyond  $10^\circ$ . In their study, the channel height was large enough that the additional confinement effects due to the protrusion of the bubbles into the channel were small.

In this paper, we will systematically change the air–water interface shape of superhydrophobic pillars in the microchannel by controlling the static pressure in the channel. In these flow geometries, unlike the work of Tsai et al. (Karatay et al. 2013; Tsai et al. 2009), confinement effect will be important. Direct measurements of the pressure drop and velocity vector field for the flow around superhydrophobic pillars will be presented for various interface shapes. These measurements will allow us to better understand and optimize the performance of superhydrophobic surfaces. Additionally, these measurements will demonstrate a novel new use for superhydrophobic surfaces as variable permeability and porosity microfluidic filters.

## 2 Experiments

A schematic diagram of the microfluidic device is shown in Fig. 1. The microchannels were produced with regular array of circular- and apple-core-shaped superhydrophobic pillars which bridge across the microchannel to create a microfluidic porous media. The microchannels were designed using AutoCAD, and a close-up of the pillar cross sections is shown in Fig. 1c, d. Each of the pillar design starts from a circular cross section with a diameter of  $D_0 = 150 \mu\text{m}$ , is spaced 375  $\mu\text{m}$  apart, and is equal in height to the microchannel at  $H = 62.2 \pm 0.1 \mu\text{m}$ . As shown in Fig. 1c, the circular cross-sectional pillar is fully wetted by the water and will be used as the control. To make superhydrophobic pillars, a number of different geometries were investigated including “x”-shaped and “+”-shaped pillars. The apple-core design shown in Fig. 1d was converged upon because of the ease of creating individual trapped bubbles along the side walls of the pillars during the initial filling of the microchannel and the longevity of the bubbles in this design. The bubbles trapped on the side of the apple-core-shaped pillars were found to last for an entire day long experiments without the needing to be replenished. To create the apple-core-shaped pillars, a circle of diameter, 35  $\mu\text{m}$ , was cut from each side of the circular pillar with the center of the cut out located at a position 47  $\mu\text{m}$  from the center of the circle. The apple-core-shaped pillars were then aligned so the shear-free air–water interface would be placed in the contraction between adjacent pillars where we expect the maximum effect on pressure drop would be produced. The microfluidic device designs were then printed on a high-resolution mask at 20,000 dpi to allow for resolution of features as small as 10  $\mu\text{m}$ . A negative of the mask was transferred to a photoresist (SU-8 2100, MicroChem) spun coat onto a silicon wafer using a mask aligner (SUSS MicroTec MA6). To form the final microfluidic devices, a casting from the master was created in polydimethylsiloxane (PDMS) (Dow Sylgard 184) (Ou et al. 2004; Whitesides and Stroock 2001), removed from the master, and bonded to a microscope glass spun coat with a thin layer of partially cured PDMS before a final bake at 60  $^\circ\text{C}$  overnight created an excellent seal (Mulligan and Rothstein 2011).

An inlet and multiple outlets were incorporated into the design at the ends of the channel as shown in Fig. 1a so that the working fluid could be driven through the device using a syringe pump. Distilled water was used as the working fluid in all experiments presented here. Four pressure ports were incorporated to read the pressure at multiple locations within the microchannel and get accurate pressure drop values. The pressure drops reported

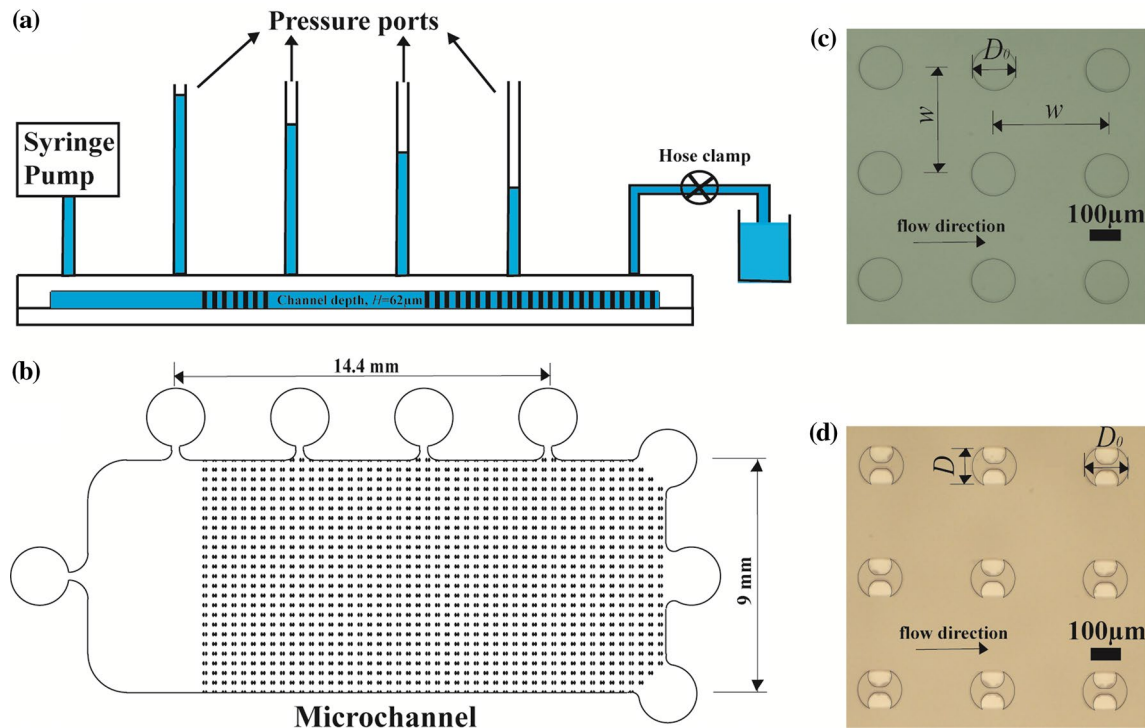


**Fig. 1** Schematic diagram of the experimental setup. Also included are **a** schematic diagram for pressure drop measurements, **b** top-down schematic diagram of the microchannel, and optical microscope

images of **c** circular pillars and **d** apple-core-shaped superhydrophobic pillars. The diameter of each pillar,  $D_0$ , is  $150\ \mu\text{m}$  and they are spaced  $375\ \mu\text{m}$  apart

here will primarily be from the most upstream and downstream ports. The two pressure ports in the middle were superfluous for pressure drop measurements, but in addition to the three outlet ports, they were extremely useful for removing unwanted air bubbles within the microfluidic device. The static pressure in the microchannel was controlled by changing the pressure drop through the outlet tubing. This was accomplished by manually tightening or loosening a hose clamp. The change in static pressure from 500 to 2500 Pa was used to change the shape of the air–water interface trapped along the superhydrophobic pillar from roughly flat,  $D/D_0 = 0.8$ , to circular,  $D/D_0 = 1.0$ , to convex,  $D/D_0 = 1.1$ . Here,  $D$  is the width of the apple-core-shaped pillar measured at the center of the trapped air–water interface. Some variation in the measured size of the trapped air bubbles was observed for the superhydrophobic pillars due to variation in the fabrication process. To minimize error, the diameter of the air bubbles was measured at 50 different superhydrophobic pillars in the microchannel. Also note that although the shape of the meniscus is uniform across most of the pillar, it does change very close to the top and bottom of the pillar where it interacts with the top and bottom wall of the PDMS microchannel.

All the pressure drop measurements were taken using manometer columns with 0.5-mm-height resolution and

were taken at a fixed volume flow rate of  $Q = 0.1\ \text{ml/min}$ . This flow rate corresponds to a capillary number of  $Ca = \mu U/\sigma = 6.6 \times 10^{-5}$  and a Reynolds number of  $Re = \rho U w/\mu = 0.71$ . The average streamwise velocity between each pillar in the microchannel,  $U_{\text{pillar}} = Q/H(w - nD_0) = 4.75\ \text{mm/s}$ , was calculated using conservation of mass, and confirmed by microparticle image velocimetry ( $\mu\text{PIV}$ ). Here,  $\mu$  is the viscosity of working fluid,  $H$  is the depth of the microchannel,  $w$  is the width of the microchannel,  $n$  is the number of pillars,  $\rho$  is the density, and  $\sigma$  is the surface tension. The depth of the microchannel was measured to be  $H = 62.2 \pm 0.1\ \mu\text{m}$  using a surface profilometer. The pressure drop of the apple-core-shaped superhydrophobic pillars was compared to that of the baseline circular pillars to evaluate the effect of air–water interface shape on the pressure drop. The maximum uncertainty of pressure drop was calculated to be 5 Pa.

To measure velocity vector fields around the circular and superhydrophobic pillars in the microchannel, microparticle image velocimetry ( $\mu\text{PIV}$ ) system was utilized. The microchannel was placed to a Nikon inverted microscope (Nikon Eclipse TE 2000-U) with a  $20\times$  objective. Fluorescent carboxylate-modified latex particles with  $1\ \mu\text{m}$  diameter (FluoSpheres) were mixed with the distilled water and driven through the microchannel at a flow rate of  $Q = 0.1\ \text{ml/min}$ . The particles absorbed blue light

from an illumination source (X-cite 120, EXFO) and emitted green light. The emission from the tracer particles was collected by a high-speed camera (Phantom V4.2) with  $512 \times 512$  pixels resolution. The sample rate of the camera was 1000 Hz, resulting in a time interval between successive images of  $\Delta t = 1$  ms. A commercial PIV software package (Davis 7.2 software, LaVision) was used to correlate the particle displacements and calculate velocity vector fields. To reduce noise, the velocity fields from 1000 individual cross-correlations were averaged to produce each vector field. The field of view for the PIV measurements is  $559 \times 559 \mu\text{m}$  so that a tight zoom could reveal the presence of slip along the air–water interface trapped within the apple-core-shaped superhydrophobic pillars. The minimum correlation window size used was  $6 \times 6$  pixels with 25% overlap to maximize spatial resolution in search of slip. The resulting vector spacing was  $4.4 \mu\text{m}$ . However, for the representational two-dimensional velocity vector fields and vorticity fields, a window size of  $16 \times 16$  pixels was chosen to increase the vector length, while avoiding vector overlap. All the velocity measurements were taken in the middle of microchannel at a depth of  $30 \mu\text{m}$ .

### 3 Results and discussion

Starting with a fresh microchannel, an air bubble was trapped within the side walls of the superhydrophobic apple-core-shaped pillars by a forced wetting process. In Fig. 2a, the dry apple-core-shaped superhydrophobic pillars are shown in the microchannel. Water was driven with a syringe pump through the microchannel. As shown in Fig. 2b, as the water advanced through the microchannel, the water was pinned and deflected at the front edges of each successive pillar. The water remained pinned until its contact angle with the pillars reached  $\theta_A = 110^\circ$  locally.

This is shown in Fig. 2b. Beyond this advancing contact angle, the air–water interface advanced along the surface of a single pillar. When the advancing water reached the upstream re-entrant corner of the cut out in the apple-core-shaped pillar, the air–water interface continued to deform, but remained pinned. The combination of the high advancing contact angle and surface tension kept the water from wetting down into the cavity within the pillar wall. As a result, as the water progressed past each successive pillar, two small bubbles of air were trapped within each apple-core-shaped pillar. The air bubbles were initially relatively small with a flat or even a concave profile; however, as the pressure of the initial flow was removed, the air bubbles expanded beyond  $D/D_0 > 1$  as shown in Fig. 2c. This is because the pressure in the air phase remains set by the local pressure during the initiation of the microchannel in Fig. 2b. As the flow was removed, the pressure in the water phase dropped and the air expanded until the internal pressure was balanced by the combination of water pressure and Laplace pressure produced by the curved air–water interface.

For comparison with the superhydrophobic pillar array, pressure drop measurements were first taken on an array of solid circular cross-sectional pillars shown in Fig. 1c. At an average velocity between the pillars of  $U_{\text{pillar}} = 4.75$  mm/s and a capillary number of  $Ca = 6.6 \times 10^{-5}$ , a pressure drop of  $\Delta P = 159.4 \pm 1.4$  Pa was measured. Note that to within the uncertainty of the measurements the pressure drop was found to be independent of the static pressure in the microfluidic device, indicating that the internal pressure within the microfluidic device did not cause an expansion or swelling of the microchannel that would bias the drag reduction measurements. Next, a series of pressure drop measurement were performed for the apple-core-shaped superhydrophobic pillar arrays to investigate the dependence of pressure drop on the shape of the trapped air–water

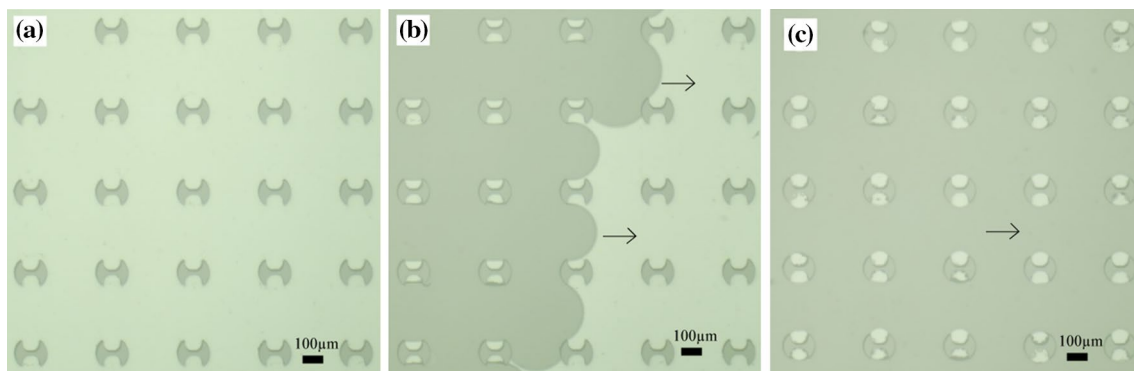


**Fig. 2** A series of microscope images showing the initialization of the microfluidic device and formation of the air–water interface in the superhydrophobic apple-core-shaped pillars at  $Ca = 6.6 \times 10^{-5}$ .

Included are images of superhydrophobic pillars **a** dry prior to flow initialization, **b** during the wetting process, and **c** fully initialized. The flow direction is from *left to right*

interface. To facilitate these measurements, the pressure drop through the downstream tubing was systematically changed with a hose clamp in order to change the static pressure in the microfluidic device without affecting the flow rate within the microchannel which was controlled independently using a syringe pump. By changing the static pressure, the curvature of the air–water interface was modulated through a range from  $D/D_0 = 0.8$  to  $D/D_0 = 1.1$ . Multiple measurements with different interface curvatures were taken with a given microfluidic device, allowing interface shape and pressure drop to reach a stable equilibrium between each pressure drop measurement. The pressure drop reduction for superhydrophobic pillars and in some cases pressure drop enhancement was calculated by comparing its pressure drop to the pressure drop across the array of circular pillars at the same velocity and capillary number. The results are shown in Fig. 3. The pressure drop reduction is defined as  $PDR = (\Delta P_{\text{circular}} - \Delta P_{\text{SHS}}) / \Delta P_{\text{circular}}$ . At  $D/D_0 = 1.0$ , where the protrusion of the air–water interface from within the apple-core-shaped pillar results in a cross-sectional shape that is identical to that of the circular pillar, a pressure drop reduction of  $PDR = 7\%$  was obtained. Although data for a normalized diameter of exactly  $D/D_0 = 1.0$  were not obtained, the pressure drop reduction at  $D/D_0 = 1.0$  was interpolated from the data by fitting lines of best fit to the measured pressure drop in Fig. 3. This result shows the impact that the presence of the fluid slip that resulting reduction of shear stress at the air–water interface can have on the flow through a micropillar

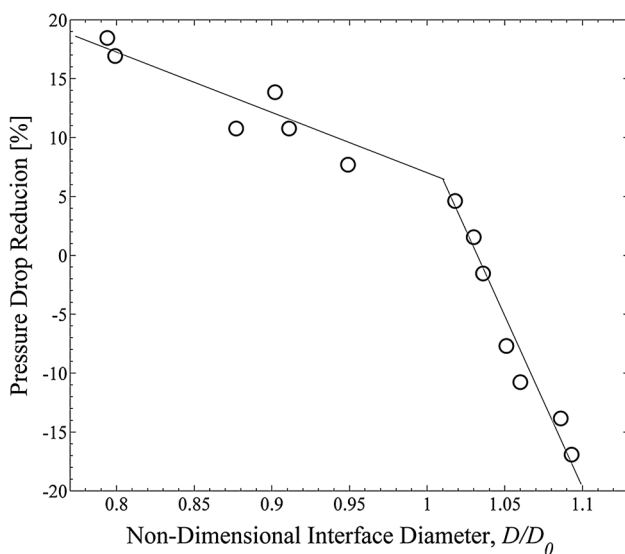


**Fig. 3** Pressure drop reduction as a function of non-dimensional interface diameter for flow through a microchannel containing a regular array of superhydrophobic apple-core-shaped pillars. The data are non-dimensionalized through comparison against an array of circular pillars with diameter  $D_0$  and include the experimental pressure drop (open circle) and linear lines fitted to the data to guide the reader's eye (line)

array. This pressure drop reduction may appear small when compared to flow across superhydrophobic surfaces with continuous slip interfaces (ridges, posts, etc.) (Ou et al. 2004; Ou and Rothstein 2005; Song et al. 2014). This is because, in our microfluidic device, the fluid experienced an additional large viscous drag from the presence of the top and bottom walls of the microchannel.

As shown in Fig. 3, the measured pressure drop reduction was found to be quite sensitive to changes in the shape of the air–water interface. By constricting the downstream tubing and raising the static pressure in the microchannel, the air–water interface trapped within the superhydrophobic pillars was compressed. At the highest pressures tested, the interface became roughly flat and aligned parallel to the flow direction for  $D/D_0 = 0.8$ . As the air pocket was compressed, the effective flow cross-sectional area between the pillars became larger. As a result, the form drag related to the pillar size and shape as well as the drag resulting from shear stress associated with the flow between pillars was reduced. Thus, the pressure drop would have become smaller due to geometry changes even in the absence of the shear-free air–water interface. A pressure drop reduction of 18% was measured for the most concave interface tested at  $D/D_0 = 0.8$ . By reducing the outlet constriction, the static pressure in the channel was reduced and the air pockets were allowed to grow beyond  $D/D_0 > 1$ . As shown in Fig. 3, a sharp decrease in the pressure drop reduction was observed with increasing non-dimensional interface diameter. In fact, beyond  $D/D_0 > 1.02$ , a negative pressure drop reduction or, in other words, a pressure drop increase was observed. As the air–water interface protruded into the water phase, it becomes an additional obstacle to fluid flow by reducing the cross-sectional area between pillars. A 17% increase in the pressure drop was observed for the largest non-dimensional interface diameter tested,  $D/D_0 = 1.1$ . Similar measurements for bubble matrices with convex air–water interfaces have been reported in the past (Karatay et al. 2013). Here, we show for both convex and concave interface shapes that the drag through a microchannel array of superhydrophobic pillars can be very sensitively controlled by the air–water interface shape.

In Fig. 3, the pressure drop through the array apple-core-shaped superhydrophobic pillars is compared against the pressure drop through the array of circular pillars. As described above, this comparison takes into account both the pressure drop reduction associated with the slip along the trapped air–water interface and the pressure drop increases/decreases due to the confinement effects resulting from the growing/shrinking of the trapped air pocket. In order to separate these two effects, a series of measurements were taken where the air–water interface was intentionally contaminated with small, one-micron-diameter particles to transform it from shear-free to no slip. The

particles used for  $\mu$ -PIV are slightly hydrophobic in nature. As a result, over time the particles can begin to accumulate along the air–water interface. Given the size of the particles, this accumulation is essentially irreversible (Zeng et al. 2006). After roughly 30 minutes,  $\mu$ -PIV confirmed that the surface coverage of the particles was sufficient to make interface immobile and could be treated as a no-slip surface. For this reason, all  $\mu$ -PIV measurements presented below were taken within the first few minutes of the onset of flow to ensure a non-contaminated, fully mobile interface. Surfaces contaminated by surfactants have also been shown to reduce interface mobility (Bolognesi et al. 2014), although it should be pointed out that no evidence for surfactant contamination was observed here.

Pressure drop measurements were then taken for a series of apple-core-shaped pillars with no-slip, particle-contaminated air–water interfaces having diameter ratios between  $0.8 < D/D_0 < 1.1$ . For  $D/D_0 = 1.0$ , the pressure drop was found to be the same as for the array of no-slip circular cylinder result within the experimental uncertainty and 7% higher than for a clean, mobile air–water interface. This gave us confidence in our approach. For  $D/D_0 = 0.86$ , the pressure drop for flow through an array of apple-core-shaped pillars with no-slip, particle-contaminated air–water interfaces was found to be 6.7% higher than for the same array of apple-core-shaped pillars with a clean, mobile air–water interfaces. This observation shows that the drag reduction observed in Fig. 3 was not entirely due to the change in shape of the pillars. For  $D/D_0 = 1.05$ , the pressure drop for flow through an array of apple-core-shaped pillars with no-slip, particle-contaminated air–water interfaces was found to be 8.4% higher than for the clean, mobile air–water interface. The data show a small, but significant, increase in reduction in the skin friction drag as the air–water interface becomes more convex. This is consistent with recent observations (Karatay et al. 2013).

In order to better understand the observed pressure drop variation with changing the air–water interface shape, detailed velocity fields around two adjacent circular and superhydrophobic pillars were measured using microparticle image velocimetry ( $\mu$ PIV). These two-dimensional vector fields were then used to study in detail the presence and effect of slip along the air–water interface trapped with the superhydrophobic pillars. This was done by examining the evolution of the velocity profiles along three different slices parallel to the flow direction as well as one slice perpendicular to the flow cutting between the centers of two adjacent pillars.

The velocity vector fields and corresponding vorticity fields around the circular and superhydrophobic apple-core-shaped pillars are presented in Fig. 4. The dimensionless interface diameter of the superhydrophobic pillars was  $D/D_0 = 0.88$  and  $D/D_0 = 1.09$ , respectively. The spatial

channel positions were non-dimensionalized by the diameter of the circular pillar,  $D_0 = 150 \mu\text{m}$ . It should be noted that due to variations in the exact interface shape, cases of superhydrophobic pillars with some modest asymmetry in the flow can be found throughout the microchannel. As shown in Fig. 4, symmetric flow was observed on both the adjacent circular and superhydrophobic pillars. In both cases, stagnation points were observed at the leading and trailing edges of the pillars. The flow was then found to accelerate into the contraction between pillars before decelerating on its way out. This acceleration and deceleration of the flow allowed the resulting streamline curvature and shear results in high vorticity areas at the top and bottom of the pillars in the throat of the contraction.

From Fig. 4, the first obvious difference between the circular and superhydrophobic pillars can be seen in the magnification of the vorticity. The maximum and extent of the vorticity for both cases of the superhydrophobic pillars were found to be smaller than those of the circular pillars. For  $D/D_0 = 0.88$ , the shape of the air–water interface was essentially flat. Thus, the curvature effect from the geometry of the interface was reduced compared to the case of the circular pillar, resulting in the decrease in the magnitude of the vorticity. As the air–water interface was increased beyond  $D/D_0 > 1$ , the vorticity is expected to increase with the increased streamline curvature and velocity in the contraction. In fact, the presence of the slip at the air–water interface was found to reduce the magnitude of the vorticity at  $D/D_0 = 1.09$  even as the pressure drop increased beyond the case of the solid circular pillar. To quantify the magnitude of the vorticity attenuation, the maximum values of vorticity around six different sets of pillars were measured and averaged. The absolute maximum of the vorticity for the superhydrophobic case was measured to be  $\omega = 134 \text{ s}^{-1}$  and  $\omega = 159 \text{ s}^{-1}$  for  $D/D_0 = 0.88$  and  $D/D_0 = 1.09$ , respectively. They correspond to 29% and 16% decrease in the vorticity for  $D/D_0 = 0.88$  and  $D/D_0 = 1.09$ , respectively, compared to the flow past a solid circular pillar for which the vorticity was found to be  $\omega = 189 \text{ s}^{-1}$ . Reduction in vorticity has been observed previously for flow past a macroscale circular cylinder with a superhydrophobic coating (Muralidhar et al. 2011). In those experiments, which were performed at large Reynolds number, the reduction in vorticity was found to delay flow separation and vortex shedding and reduce the magnitude of the time periodic lift force (Daniello et al. 2013).

In Fig. 5, streamwise velocity measurements are presented for both the circular pillars and the apple-core-shaped superhydrophobic pillars along the three different slices between the two pillars parallel to the flow direction. In all the cases, the streamwise velocities were non-dimensionalized by the average streamwise velocity of the water between two pillars,  $U_{\text{pillar}} = 4.75 \text{ mm/s}$ . A schematic

**Fig. 4** Particle image velocimetry (PIV) vector fields of flow through a regular array of **a** circular and **b, c** superhydrophobic apple-core-shaped pillars at  $Ca = 6.6 \times 10^{-5}$  with vorticity overlaid as a contour map. *Solid lines* are overlaid on the data to indicate the position of pillars while *dotted lines* are used to represent the position of the air–water interface formed by the air bubble trapped against the superhydrophobic pillar. For the superhydrophobic pillar, the non-dimensional diameter was measured to be **b**  $D/D_0 = 0.88$  and **c**  $D/D_0 = 1.09$  from bright-field image

diagram is inserted into Fig. 5 to show the locations of the horizontal measurement slices. The first slice in Fig. 5a is located along the centerline between the two adjacent pillars. A subsequent slice in Fig. 5b is located at the bottom edge of the circular pillar or, for the case of two superhydrophobic pillars, at the edge of the air–water interface of the upper pillar. And, the slice in Fig. 5c is located along a horizontal slice 4.4  $\mu\text{m}$  from the slice in Fig. 5b closer to the centerline.

As shown in Fig. 5a, along the centerline between the two pillars, the streamwise velocity was found to accelerate by 34% from  $u/U_{\text{pillar}} = 0.95$  to  $u/U_{\text{pillar}} = 1.27$  for flow through the array of circular pillars. However, as the air–water interface was expanded from  $D/D_0 = 0.8$  to  $D/D_0 = 1.09$ , the magnitude of the acceleration in the streamwise velocity was found to grow by 41% from  $u/U_{\text{pillar}} = 0.92$  to  $u/U_{\text{pillar}} = 1.30$  for the  $D/D_0 = 1.09$  case. The increase in the maximum velocities of the flow between the superhydrophobic pillars for  $D/D_0 = 1.09$  was larger than that of the circular pillars for two reasons. First, there was a larger confinement effect which drove the velocity up simply due to conservation of mass. Note, integrating the velocity profile along any vertical slice confirms conservation of mass for flow through arrays of both circular- and apple-core-shaped superhydrophobic pillars within a couple of percent. Second, as we will see, there is a significant slip velocity along the air–water interface trapped against the apple-core-shaped superhydrophobic pillar which affects the velocity profiles between the superhydrophobic apple-core-shaped pillars.

Even more significant variations in the streamwise velocities can be observed for slices taken very near the solid and apple-core-shaped superhydrophobic pillars. As shown in Fig. 5b, the streamwise velocity profile past both the circular and superhydrophobic pillars decreased from nearly  $u/U_{\text{pillar}} = 0.7$  far upstream of the pillars to a minimum at the narrowest point in the centerline and increased downstream of the pillars back to  $u/U_{\text{pillar}} = 0.7$ . For the slice that passes through the edge of the circular pillar, the streamwise velocity was found to go to zero, thus confirming the no-slip condition at the solid surface. For the superhydrophobic apple-core-shaped pillars, a significant slip velocity was observed along the trapped air–water interface.

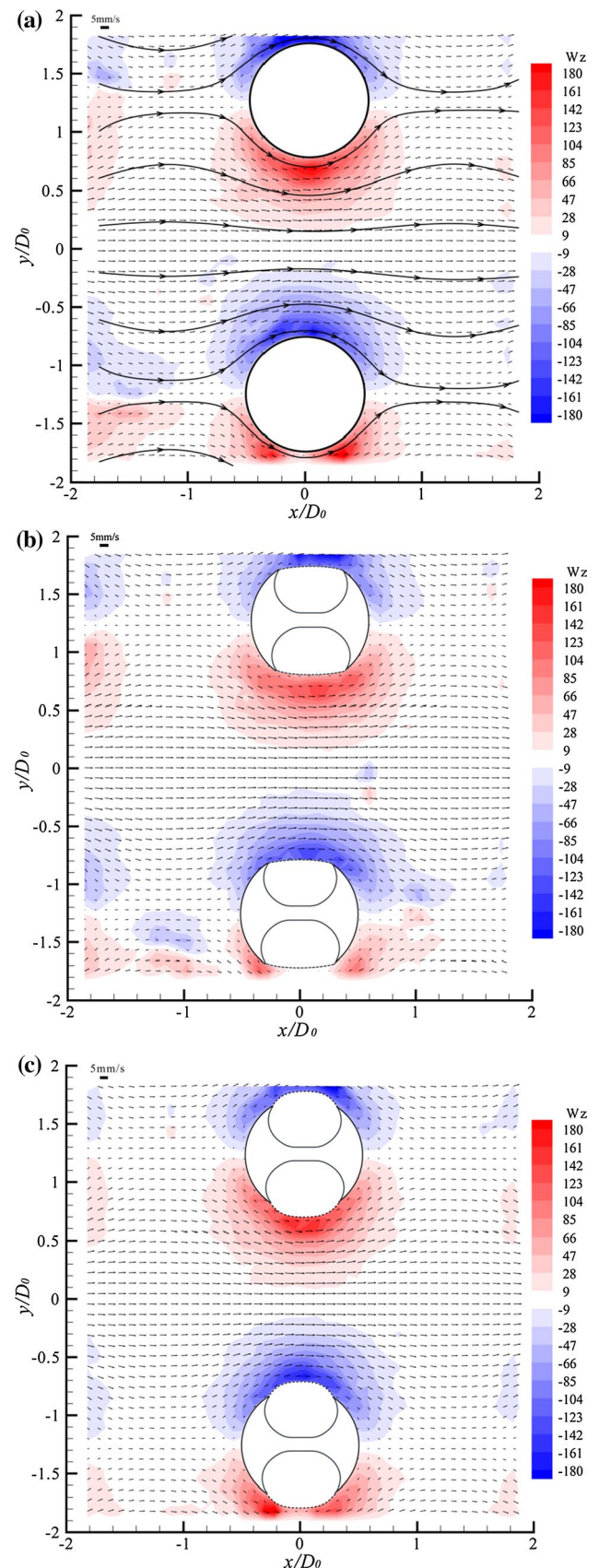
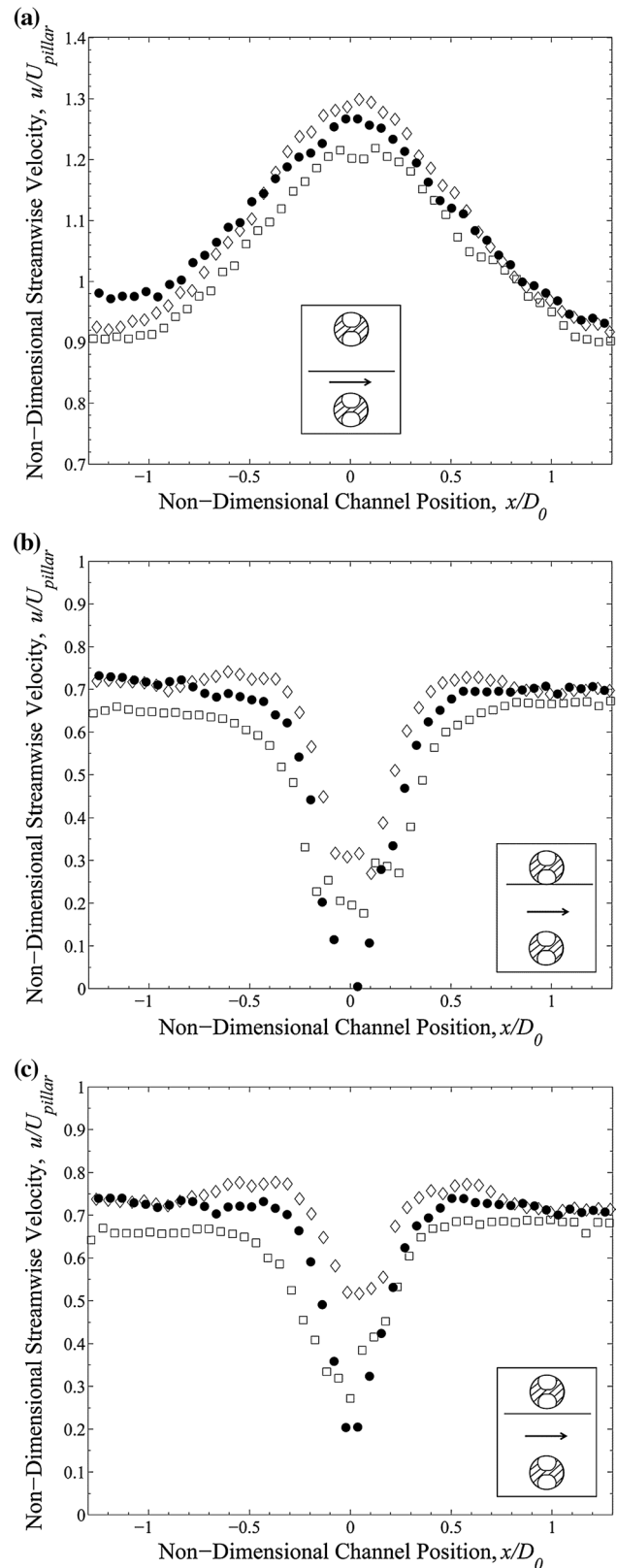


**Fig. 5** Non-dimensional streamwise velocity as a function of non-dimensional channel position,  $x/D_0$ . The streamwise velocities were measured **a** along the centerline between two pillars, **b** at the edge of the solid surface or air–water interface of the upper pillar, and **c** at a position  $4.4 \mu\text{m}$  below the edge of the upper pillar. The experimental data include the velocity measured in the microchannel with the circular pillars (*filled circle*) and the superhydrophobic apple-core-shaped pillars with  $D/D_0 = 0.88$  (*open square*) and  $D/D_0 = 1.09$  (*open diamond*). The velocity was non-dimensionalized by the average streamwise velocity in the microchannel,  $u/U_{\text{pillar}}$ . *Inset* shows the locations of the measurement slices in relation to the two pillars

The evolution of the velocity profiles obtained for the superhydrophobic apple-core-shaped pillars was quite different in two important ways. First, as the non-dimensional interface diameter was increased to  $D/D_0 = 1.09$ , the streamwise velocity was found to increase slightly from  $u/U_{\text{pillar}} = 0.69$  to  $u/U_{\text{pillar}} = 0.73$  just upstream and downstream of the pillars at  $D/D_0 = \pm 0.7$  as shown in Fig. 5b. This could be due to the slight differences in the pillar cross-sectional geometry as the air bubble attached to the superhydrophobic pillar in this case protruded out beyond extent of the circular pillar to a width of  $D/D_0 = 1.09$ , resulting in a slightly non-circular shape which could modify the local velocity profile. This flow phenomenon is more prevalent for the data in the slice taken  $4.4 \mu\text{m}$  away from the air–water interface as shown in Fig. 5c. Note that when the non-dimensional interface diameter was smaller than one,  $D/D_0 < 1$ , the increase in the streamwise velocity was not observed near the edge of the air–water interface due to the decrease in the effective pillar size. Second, at the throat, the streamwise velocity past the superhydrophobic pillars did not go to zero, but instead it showed a pronounced slip velocity of approximately 20% of  $U_{\text{pillar}}$  for the  $D/D_0 = 0.88$  case and 30% of  $U_{\text{pillar}}$  for the  $D/D_0 = 1.09$  case. This result clearly demonstrates that the slip velocity at the interface is sensitive to interface curvature and, for this geometry at least, increases with increasing protrusion angle of the air–water interface protrudes into the water phase. These observations are consistent with previous measurements of flow past bubble matrices. This increase in the slip velocity with air bubble protrusion will be discussed in more detail in the paragraphs that follow.

For the PIV measurements presented in Fig. 5, the final computation window size was  $6 \times 6$  pixels, resulting in a vector spacing of  $4.4 \mu\text{m}$ . In order to accurately report a slip velocity, the position of the solid–water interface of the circular pillars and the air–water interface of the superhydrophobic pillars must be very accurately known. To find their location, bright-field images were used to accurately determine the position of the solid–water and air–water interfaces within a single pixel (or  $1 \mu\text{m}$ ) using ImageJ. Once the location of the interface was obtained, the slip velocity at the interface was determined by fitting the six velocity



data points closest to the interface with a second-order polynomial and extrapolating the fit to the interface. In Fig. 6, the streamwise velocity profile measured along a vertical/

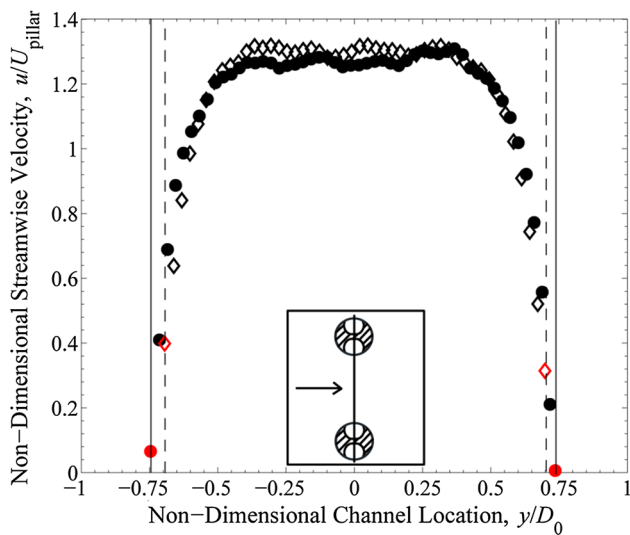


**Fig. 6** Non-dimensional streamwise velocity  $u/U_{\text{pillar}}$  as a function of non-dimensional channel location for velocities evaluated along  $x/D_0 = 0$ . The experimental data include velocity profiles for circular pillars (filled circle) and superhydrophobic pillars with  $D/D_0 = 1.09$  (open diamond). The slip velocity data are superimposed on the interface lines with red symbols. The vertical solid lines at  $y/D_0 = \pm 0.75$  represent the edge of the circular pillar while the dashed lines at  $y/D_0 = \pm 0.7$  represent the location of the air–water interface formed around the superhydrophobic pillar (colour figure online)

cross flow slice connecting the centers of the two pillars is shown. The solid vertical lines at  $y/D_0 = \pm 0.75$  indicate the edge of the circular pillar while the vertical dashed lines at  $y/D_0 = \pm 0.7$  indicate the position of air–water interface trapped within the superhydrophobic apple-core-shaped pillar. The slip velocity data extrapolated from the second-order fits are superimposed on the interface lines.

For both the circular and superhydrophobic pillars, the streamwise velocities were found to remain nearly constant away from the walls between the two adjacent pillars. This is consistent with flow through rectangular channels where the height is significantly smaller than the width as it is here. The velocity was found to decrease sharply with a large velocity gradient near the pillars. The velocity at the solid circular pillar was found to be zero within the uncertainty of the velocity and wall position, confirming the no-slip boundary condition. However, the velocity at the air–water interface of the superhydrophobic pillars was measured to be nonzero with an average value of  $U_{\text{slip}} = 1.7 \pm 0.2$  mm/s at  $D/D_0 = 1.09$ , as shown in Fig. 6. This slip velocity corresponds to  $U_{\text{slip}}/U_{\text{pillar}} = 36\%$  the average streamwise velocity between pillars. Given the spatial uncertainty of the interface location and the error of the velocity measurements, the data are known with an uncertainty of  $\pm 0.3$  mm/s.

From the PIV vector fields in Fig. 4, it is possible to measure the velocity at multiple locations along the

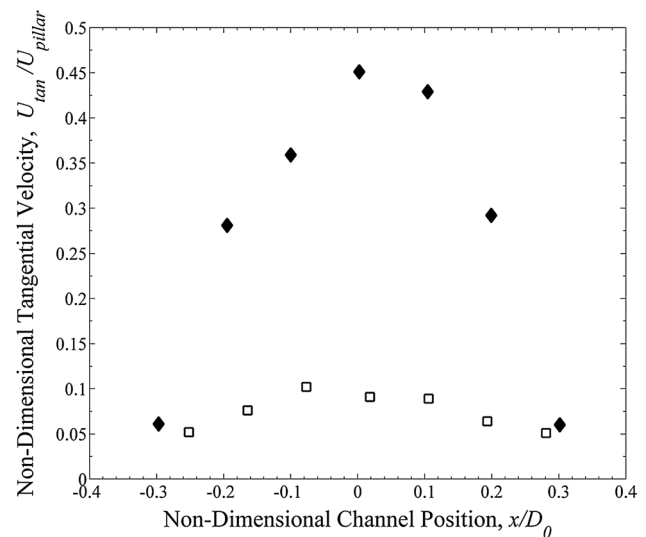


**Fig. 7** Non-dimensional tangential velocity,  $U_{\text{tan}}/U_{\text{pillar}}$ , measured along the air–water interface as a function of non-dimensional channel position,  $x/D_0$ . The experimental data include velocity for the superhydrophobic pillar with  $D/D_0 = 0.88$  (open square) and  $D/D_0 = 1.09$  (filled diamond)

air–water interface trapped within the apple-core-shaped superhydrophobic pillars. This is presented in Fig. 7 for the two most distinguished interfaces shown here:  $D/D_0 = 0.88$  and  $D/D_0 = 1.09$ . In Fig. 7, measurements of the tangential velocity are presented at seven different points along the interface. In both cases, the tangential velocity was found to increase from roughly zero at the leading edge of the air–water interface to a maximum slip velocity at the midpoint of the interface after which it decreased back to zero at the downstream edge of the air–water interface. As expected, the slip velocity was found to approach zero at the leading and trailing edges of the interface where the presence of the solid corner of the pillar enforces the no-slip boundary condition. As was seen in Ou and Rothstein's work (2005), the slip velocity along the interface was found to be roughly parabolic. As noted previously, the maximum tangential slip velocity increased dramatically with increasing interface expansion. At  $D/D_0 = 1.09$ , a maximum of  $U_{\text{tan}}/U_{\text{pillar}} = 45\%$  was found while a maximum tangential slip velocity along the interface of only  $U_{\text{tan}}/U_{\text{pillar}} = 10\%$  was found for the case of  $D/D_0 = 0.88$ . Some fluctuation in the values was observed from pillar to pillar so the results were compared for flow between several superhydrophobic pillars. As the shape of the air–water interface was expanded, the averaged maximum tangential velocity at the midpoint of the interface was measured to be  $U_{\text{tan}}/U_{\text{pillar}} = 5 \pm 3\%$ ,  $20 \pm 2\%$ ,  $24 \pm 1\%$ , and  $36 \pm 4\%$  for  $D/D_0 = 0.88, 0.98, 1.05,$  and  $1.09$ , respectively. From this measurement, it is clear that the increase in the effective size of the superhydrophobic pillar not only increased

the pressure drop in the channel due to enhanced confinement and form drag, but also enhanced slippage along the air–water interface reducing the friction drag along the superhydrophobic pillars. For the cases where  $D/D_0 > 1.03$ , the geometry effect of the expanded convex air–water interface was found to dominate the flow even as the slippage effect at the air–water interface grew with increasing bubble size. This is one reason why the pressure drop reduction to was found to increase with increasing non-dimensional interface diameter,  $D/D_0$ , when the data was compared not against the data for the circular pillar, but apple-core-shaped pillars having a particle-contaminated no-slip interface with the same cross-sectional shape.

#### 4 Conclusions

The pressure drop and velocity vector fields for the flow past a regular array of superhydrophobic apple-core-shaped pillars in the microchannel were measured to investigate the role of the interface shape on laminar drag reduction. A series of PDMS microchannels with the apple-core-shaped and circular pillars were prepared and tested at a capillary number of  $Ca = 6.6 \times 10^{-5}$ . The air bubbles were trapped along the sides of each superhydrophobic apple-core-shaped pillar during the initial filling of the microchannel due to combination of the hydrophobicity of the PDMS and the geometry of the pillar which contains a re-entrant corner. The air–water interface was systematically changed from a concave to a convex shape by changing the static pressure in the microchannel.

The pressure drop through the microchannel containing superhydrophobic pillars was found to depend on the shape of the trapped air–water interface. As the interface was compressed into the superhydrophobic pillar becoming concave, the cross-sectional area between adjacent pillars became larger while a significant slip velocity was introduced along the air–water interface. The result was a significant decrease in the measured pressure drop. The pressure drop reduction increased with decreasing non-dimensional interface diameter,  $D/D_0$ . For the most concave interface tested for  $D/D_0 = 0.8$ , an 18% reduction in the pressure drop compared to the solid circular pillars was found. Of that pressure drop reduction, 6% was due to reduction in skin friction and 12% was due to a reduction in form drag. For convex interfaces, the pressure drop was found to grow with increasing protrusion of the interface into the gaps between adjacent pillars. At  $D/D_0 = 1.1$ , an increase of 17% in the pressure drop compared to the flow through an array of solid circular pillars was found due primarily to a decrease in the effective cross-sectional area between pillars due to an increase in the effective size of the superhydrophobic pillar. Slip was found to counteract

the increase in form drag due to the convex air–water interface. The presence of the air–water interface was shown to reduce the drag by approximately 9% while the increased confinement effects resulting from the protruding air were found to increase the pressure drop by 26% for this case. When the diameter of the air bubbles trapped within the superhydrophobic pillars was the same as the diameter of the circular pillars,  $D/D_0 = 1.0$ , a 7% pressure drop reduction was obtained as a result of the presence of a significant slip velocity along the air–water interface.

From the PIV measurements of velocity vector fields through these pillar arrays, the detailed fluid dynamics around the circular and superhydrophobic pillars were studied and qualitatively compared. The presence of the array of pillars induced an acceleration of the flow into the contraction between two pillars and a deceleration exiting the contraction. The result was the formation of a high vorticity region at the top and the bottom of both the circular and superhydrophobic pillars. When compared to the circular pillars, the intensity of the vorticity was attenuated for all cases of the superhydrophobic pillars both concave and convex. When the non-dimensional interface diameter was less than one,  $D/D_0 < 1$ , the reduction in shear stress along the air–water interface due to slip coupled with the simultaneous reduction in a vorticity generation due to streamline curvature was found to lead to a decrease in vorticity below the value observed for a solid circular pillar. However, as the interface diameter was increased beyond  $D/D_0 > 1$  and up to  $D/D_0 = 1.1$ , the presence of slip at the air–water interface was found to reduce the measured vorticity below the value of the circular pillars even as the increased streamline curvature drove the vorticity up.

A slip velocity along the air–water interface was found to exist in the apple-core-shaped superhydrophobic pillars for all the non-dimensional interface diameters tested. However, the slip velocity was found to be strongly dependent on the curvature of the trapped air–water interface. The maximum slip velocity was always found to exist at the midpoint of the air–water interface independent of interface shape. Additionally, the slip velocity was found to increase as the interface grew from concave to flat and finally to convex as it expanded into opening between adjacent pillars. For the most convex interface tested,  $D/D_0 = 1.09$ , the maximum tangential velocity was measured to be 45% of the average streamwise velocity between adjacent pillars in the channel. Interestingly, even though this case was found to have the largest slip velocity and the largest reduction in skin friction drag, it resulted in a pressure drop increase due to confinement effects.

Throughout a series of measurements for pressure drop and velocity vector fields, it is clear that both the geometry and slippage of the air–water interface played important role in laminar drag reduction in the microchannel. When

the interface diameter of the superhydrophobic apple-core-shaped pillars was the same with the diameter of the circular pillar, the presence of the slip at the air–water interface led to a pressure drop reduction. As the interface diameter was increased, the decrease in the cross-sectional area between adjacent pillars led to an increase in the pressure drop even as the slip velocity along the air–water interface increased monotonically with the increasing trapped air bubble size and increasing convex curvature of the interface.

**Acknowledgements** This research was supported by the National Science Foundation under Grant CBET-1334962.

## References

- Balasubramanian AK, Miller AC, Rediniotis OK (2004) Microstructured hydrophobic skin for hydrodynamic drag reduction. *AIAA J* 42:411–414
- Bolognesi G, Cottin-Bizonne C, Pirat C (2014) Evidence of slippage breakdown for a superhydrophobic microchannel. *Phys Fluids* 26:082004
- Choi CH, Kim CJ (2006) Large slip of aqueous liquid flow over a nanoengineered superhydrophobic surface. *Phys Rev Lett* 96:066001
- Daniello R, Waterhouse NE, Rothstein JP (2009) Turbulent drag reduction using superhydrophobic surfaces. *Phys Fluids* 21:085103
- Daniello R, Muralidhar P, Carron N, Greene M, Rothstein JP (2013) Influence of slip on vortex induced motion of a superhydrophobic cylinder. *J Fluid Struct* 42:358–368
- Davis AMJ, Lauga E (2009) Geometric transition in friction for flow over a bubble mattress. *Phys Fluids* 21:011701
- Elbing BR, Winkel ES, Lay KA, Ceccio SL, Dowling DR, Perlin M (2008) Bubble-induced skin-friction drag reduction and the abrupt transition to air-layer drag reduction. *J Fluid Mech* 612:201–236
- Gogte S, Vorobieff P, Truesdell R, Mammoli A, van Swol F, Shah P, Brinker CJ (2005) Effective slip on textured superhydrophobic surfaces. *Phys Fluids* 17:051701
- Karatay E, Haase AS, Visser CW, Sun C, Lohse D, Tsai PA, Lammertink RGH (2013) Control of slippage with tunable bubble mattresses. *PNAS* 110:8422–8426
- Kim J-H, Kavehpour HP, Rothstein JP (2015) Dynamic contact angle measurements on superhydrophobic surfaces. *Phys Fluids* 27:032107
- Legendre D, Lauga E, Magnaudet J (2009) Influence of slip on the dynamics of two-dimensional wakes. *J Fluid Mech* 633:437–447
- McHale G, Shirtcliffe NJ, Evans CR, Newton MI (2009) Terminal velocity and drag reduction measurements on superhydrophobic spheres. *Appl Phys Lett* 94:064104
- Mulligan MK, Rothstein JP (2011) Deformation and breakup of micro- and nano-particle stabilized droplets in microfluidic extensional flows. *Langmuir* 27:9760–9768
- Muralidhar P, Ferrer N, Daniello R, Rothstein JP (2011) Influence of slip on the flow past superhydrophobic circular cylinders. *J Fluid Mech* 680:459–476
- Oner D, McCarthy TJ (2000) Ultrahydrophobic surfaces: effects of topography length scales on wettability. *Langmuir* 16:7777–7782
- Ou J, Rothstein JP (2005) Direct velocity measurements of the flow past drag-reducing ultrahydrophobic surfaces. *Phys Fluids* 17:103606
- Ou J, Perot JB, Rothstein JP (2004) Laminar drag reduction in microchannels using ultrahydrophobic surfaces. *Phys Fluids* 16:4635–4660
- Richardson S (1973) On the no-slip boundary condition. *J Fluid Mech* 59:707–719
- Rothstein JP (2010) Slip on superhydrophobic surfaces. *Annu Rev Fluid Mech* 42:89–109
- Sanders WC, Winkel ES, Dowling DR, Perlin M, Ceccio SL (2006) Bubble friction drag reduction in a high-reynolds-number flat-plate turbulent boundary layer. *J Fluid Mech* 552:353–380
- Sbragaglia M, Prosperetti A (2007) A note on the effective slip properties for microchannel flows with ultrahydrophobic surfaces. *Phys Fluids* 19:043603
- Song D, Daniello R, Rothstein JP (2014) Drag reduction using superhydrophobic sanded Teflon surfaces. *Exp Fluids* 55:1783
- Srinivasan S, Choi W, Park K-C, Chhatre SS, Cohen RE, McKinley GH (2013) Drag reduction for viscous laminar flow on spray-coated non-wetting surfaces. *Soft Matter* 9:5691–5702
- Steinberger A, Cottin-Bizonne C, Kleimann P, Charlaix E (2007) High friction on a bubble mattress. *Nat Mater* 6:665–668
- Truesdell R, Mammoli A, Vorobieff P, van Swol P, Brinker CJ (2006) Drag reduction on a patterned superhydrophobic surface. *Phys Rev Lett* 97:044504
- Tsai P, Peters AM, Pirat C, Wessling M, Lammertink RGH, Lohse D (2009) Quantifying effective slip length over micropatterned hydrophobic surfaces. *Phys Fluids* 21:112002
- Watanabe K, Udagawa Y, Udagawa H (1999) Drag reduction of Newtonian fluid in a circular pipe with highly water-repellent wall. *J Fluid Mech* 381:225–238
- White CM, Mungal MG (2008) Mechanics and prediction of turbulent drag reduction with polymer additives. *Annu Rev Fluid Mech* 40:235–256
- Whitesides G, Stroock AD (2001) Flexible methods for microfluidics. *Phys Today* 54:42–48
- You D, Moin P (2007) Effects of hydrophobic surfaces on the drag and lift of a circular cylinder. *Phys Fluids* 19:081701
- Zeng C, Bissig H, Dinsmore AD (2006) Particles on droplets: from fundamental physics to novel materials. *Solid State Commun* 139:547–556